AGH University of Science and Technology
Faculty of physics and Applied Computer Science

Engineering thesis

Paula Pniewska

major: **technical physics**

Search for di-Higgs production with leptons in the final state in the ATLAS experiment

Supervisor: **dr Bartłomiej Żabiński**

Cracow, January 2020

Aware of criminal liability for making untrue statements I decleare that the following thesis was written personally by myself and that I did not use any sources but the ones mentioned in the dissertation itself.

Supervisor's review

Reviewers's review

Contents

1 Introduction

1.1 The Standard Model and the Higgs boson

The Higgs boson is an elementary particle predicted by the Standard Model (SM) [1]. The existence of this particle was confirmed in 2012 as a result of ATLAS [2] and CMS [3] collaborations. The experiments were conducted at the Large Hadron Collider (LHC) [4] using proton–proton collisions. The SM is an essential theory of particle physics describing fundamental particles and the way they interact. It specifies two groups of elementary particles: fundamental fermions - building blocks of matter, and fundamental bosons - carriers of interactions. We have 12 elementary fermions of spin 1/2 fulfilling the Pauli exclusion principle which are divided into two subgroups: leptons and quarks. They are all organized into three generations - particles belonging to the first generation are the lightest and most stable, whereas the higher generations comprise particles of higher masses and lower stability. All leptons and their basic properties are shown in Table 1.1.

Table 1.1: Fundamental fermions with their masses and charges in elementary charge units [6].

	generation		
	I	II	III
leptons	electron 0.511 MeV/c^2, -e	muon 105.7 MeV/c^2, -e	tau 1.777 GeV/c^2, -e
	electron neutrino $<$2.2 eV/c^2, 0e	muon neutrino 0.17 MeV/c^2, 0e	tau neutrino $<$15.5 MeV/c^2, 0e
quarks	up $\approx$ 2.3 MeV/c^2, 2/3e	charm $\approx$ 1.275 GeV/c^2, 2/3e	top $\approx$ 173.07 GeV/c^2, 2/3e
	down $\approx$ 4.8 MeV/c^2, -1/3e	strange $\approx$ 95 MeV/c^2, -1/3e	bottom $\approx$ 4.18 MeV/c^2, -1/3e

Another group, called gauge bosons, is responsible for mediating three of the four fundamental interactions. Each fundamental force is associated with a particular boson - gluons provide the strong forces that connect quarks forming hadrons, photons mediate the electromagnetic force between electrically charged particles, whereas W and Z bosons are carriers of weak interactions. All bosons with their basic properties are presented in Table 1.2. The SM does not include gravity. However there is a hypothetical particle called *graviton* [5] which is thought to be responsible for mediating gravity forces.

Table 1.2: Basic properties of fundamental bosons [6].

	gauge (vector)	bosons			scalar bosons
name	gluon g	photon γ	W boson	Z boson	Higgs boson h
mass [GeV/c^2]	0	0	80.38	91.19	125.09
electric charge [e]	0	0	$\pm$ 1	0	0
spin	1	1	1	1	0

The Higgs boson is an essential constituent of the SM, because it explains why the other elementary particles (except photons, gluons and neutrinos) are massive. All the above mentioned bosons correspond to the vector fields. Therefore, they have spin 1. The Higgs boson is an excitation of a scalar Higgs field, so it has spin 0. It has a mass of 125.09 GeV [7] and no electric charge.

The W and Z bosons were considered in the SM theory to be massless, although measurements showed that in fact they have a non-zero mass. A solution to this problem was given by the Brout-Englert-Higgs (BEH) mechanism [8]. The Higgs field permeates the whole universe whilst particles such as quarks, leptons and W and Z bosons interact with this field acquiring mass. On the other hand, photons and gluons do not evince interactions with Higgs field. Hence, they have no mass.

1.2 Double Higgs production

The SM is an underlying theory immensely widening our understanding of the subatomic world. Nevertheless, it is incomplete. The SM does not explain gravity, neutrino masses, matter-antimatter asymmetry, or the nature of dark matter and dark energy.

Exploring the double Higgs production process could shed some light on physics beyond the Standard Model (BSM). The non-resonant production of a pair of Higgs bosons is predicted to occur very rarely in proton-proton collisions. In the SM the main production mode is the process of gluon-gluon fusion (ggF). There are two dominant contributions to this process depicted in Figure 1.1. The first one is based on Higgs boson pair production through the exchange of a virtual Higgs boson and is called a *triangle diagram*, whereas the second one includes a heavy quark (top or bottom quark) loop with two fermion–fermion–Higgs vertices and is called a *box diagram*.

The measurement of the non-resonant di-Higgs production at the LHC stands as an important test of the BEH mechanism and allows us to deepen our knowledge about the Higgs self-coupling [9]. BSM theories anticipate new options for Higgs pair production. New models embrace modifications of the Higgs boson self-coupling, existance of new heavy particles decaying into a pair of Higgs bosons and possibilities of new contact interactions between two quarks or gluons and two Higgs bosons. In particular, the production cross section for Higgs boson pairs in the SM is significantly smaller than predicted by BSM theories.

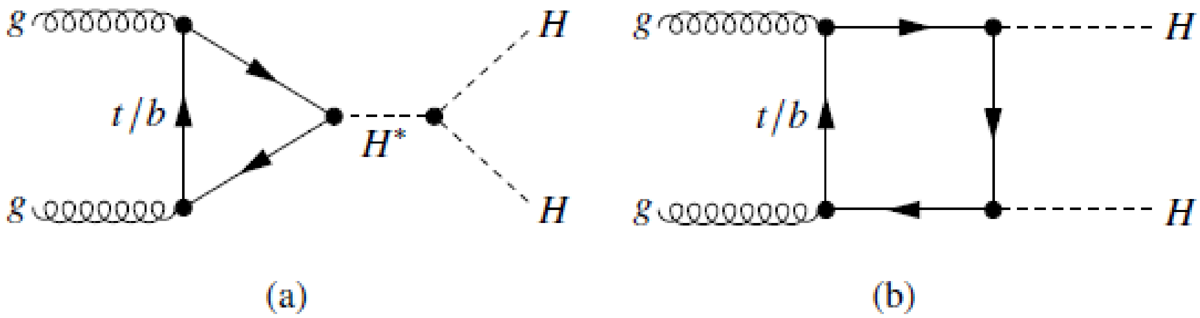

Figure 1.1: Examples of Feynman diagrams for non-resonant Higgs boson pair production in ggF process: (a) the Higgs self-coupling and (b) the heavy-quark loop [10].

1.3 Di-Higgs decay channels

The mean lifetime of Higgs boson predicted by the SM is extremely short $(1.56 \cdot 10^{-22}$ s) thus it immediately decays. There are several decay modes of the Higgs boson. Possible products of its decay are pairs of fermions or gauge bosons as shown in Figure 1.2.

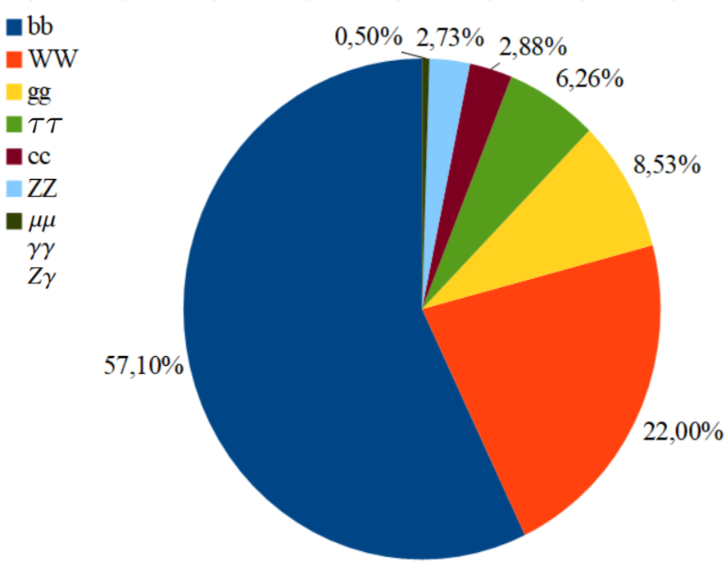

Figure 1.2: Branching ratios of single Higgs boson decay channels [11].

Combination of single Higgs decay modes leads to many di-Higgs final state possibilities. The ATLAS and CMS collaborations have performed searches for non-resonant Higgs pair production in a variety of final states. However, no significant excess beyond SM expectations is observed in these searches. The combined observed limit at 95% confidence level on non-resonant Higgs boson pair production is 6.9 times the predicted SM cross-section [12]. Possible decay channels of double Higgs and their branching fractions are collected in Table

1.3. The search for di-Higgs described in the following chapters focuses on channels including combinations of WW, $\tau\tau$ and ZZ decay modes (marked in pink in Table 1.3).

Table 1.3: Branching ratios of di-Higgs decay channels [6].

HH decay modes [%[	bb	WW	$\tau\tau$	ZZ	$\gamma\gamma$
bb	30				
WW	25	4.6			
$\tau\tau$	7.4	2.5	0.39		
ZZ	3.1	1.2	0.34	0.076	
$\gamma\gamma$	0.26	0.1	0.029	0.013	0.0005

The advantage of searching for di-Higgs with four b quarks in the final state is that this decay mode has the highest branching ratio. However, this channel suffers from a large multijet background. Decay channels with a pair of photons are much easier to select from background, but unfortunately they rarely occur.

This thesis aims to analyse multileptonic decays of double Higgs focusing on final states with one light lepton (e/μ) and one τ lepton decaying hadronically. This channel has never been studied by the ATLAS collaboration.

1.4 ATLAS detector

The ATLAS detector [13] is the largest general-purpose particle detector at the LHC at CERN. Its investigations involve SM issues, but it was mainly designed to search for phenomena of BSM physics. The ATLAS detector is cylindrical in shape, 44 metres long, 25 metres in diameter, and weighs about 7,000 tonnes. It surrounds nearly the full solid angle around the interaction point. The ATLAS detector consists of an inner tracking detector, electromagnetic and hadronic calorimeters and a muon spectrometer. The main components of the ATLAS detector are presented in Figure 1.3.

1.4.1 Coordinate system

Understanding of the coordinate system is necessary for understanding the parameters used for the analysis. The movement of the particles in the ATLAS detector is described using the cylindrical coordinate system. The interaction point is assumed to be the origin of the coordinate system, and the longitudinal axis z runs along the trajectory of the beams. The x axis points into the centre of the collider ring, and y axis points upward. The xy plane is perpendicular to the z axis. This transverse plane is described using the radial distance r (distance from the z axis) and azimuthal angle ϕ (angle around the beamline). The polar angle θ is measured from the z axis. The polar angle is used to introduce pseudorapidity $\eta = -\ln\tan(\frac{\theta}{2})$. Another parameter ΔR, is defined using η and ϕ: $\Delta R = \sqrt{\Delta\eta^2 + \Delta\phi^2}$, where $\Delta\eta$ and $\Delta\phi$ are the differences between two objects in η and ϕ respectively: $\Delta\eta = \eta_1 - \eta_2$ and $\Delta\phi = \phi_1 - \phi_2$. The ΔR could be understood as a cone that stores the information how

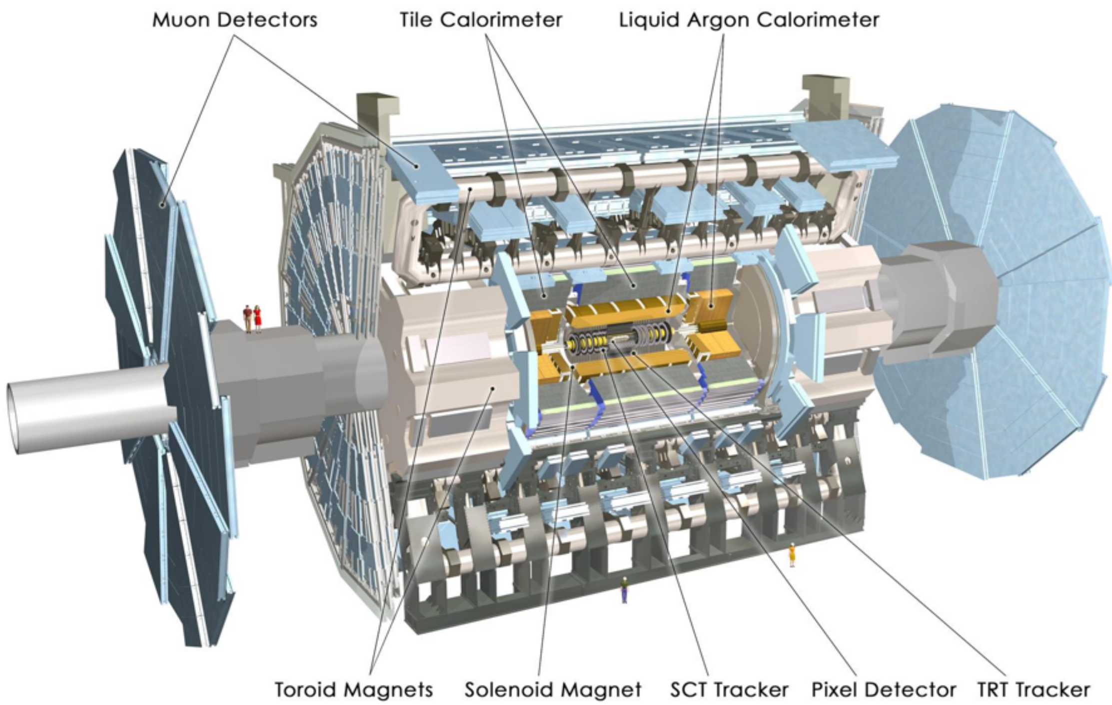

Figure 1.3: Major components of the ATLAS detector [13].

close particles are to each other. This variable indicates the level of separation between objects in the detector.

1.4.2 The inner detector

The inner detector (ID) is located close to the beam axis and is responsible for detecting the trajectories of charged particles. The ID is built of three components as presented in Figure 1.4.

The pixel detector The innermost part of the tracking system using silicone as a detecting material. It consist of 4 barrel layers with 1456 modules and 3 disks with 288 modules on the end-caps. Each of the 1744 modules has 46,080 readout channels (pixels) which gives around 80 million readout channels in total. The first layer of the ID, located approximately 3 cm from the beamline, is the Insertable B-Layer (IBL).

The semiconductor tracker (SCT) Its function is similar to the Pixel Detector though it covers a larger area and tracking is obtained through silicon microstrips. It consist of 4 barrel layers and 18 endcap discs.

The transition radiation tracker (TRT) The TRT is the outermost part of the ATLAS tracking system. Its basic elements are straw tubes of 4 mm diameter. There are around 250 thousand straws in the barrel region and 50 thousand straws in the endcaps.

Its precision is not as high as the Pixel Detector and SCT's precision but it provides some additional information about the type of the particle.

The pixel detector and the SCT cover the pseudorapidity region $\eta \leq 2.5$ and the TRT covers the region $\eta \leq 2.0$.

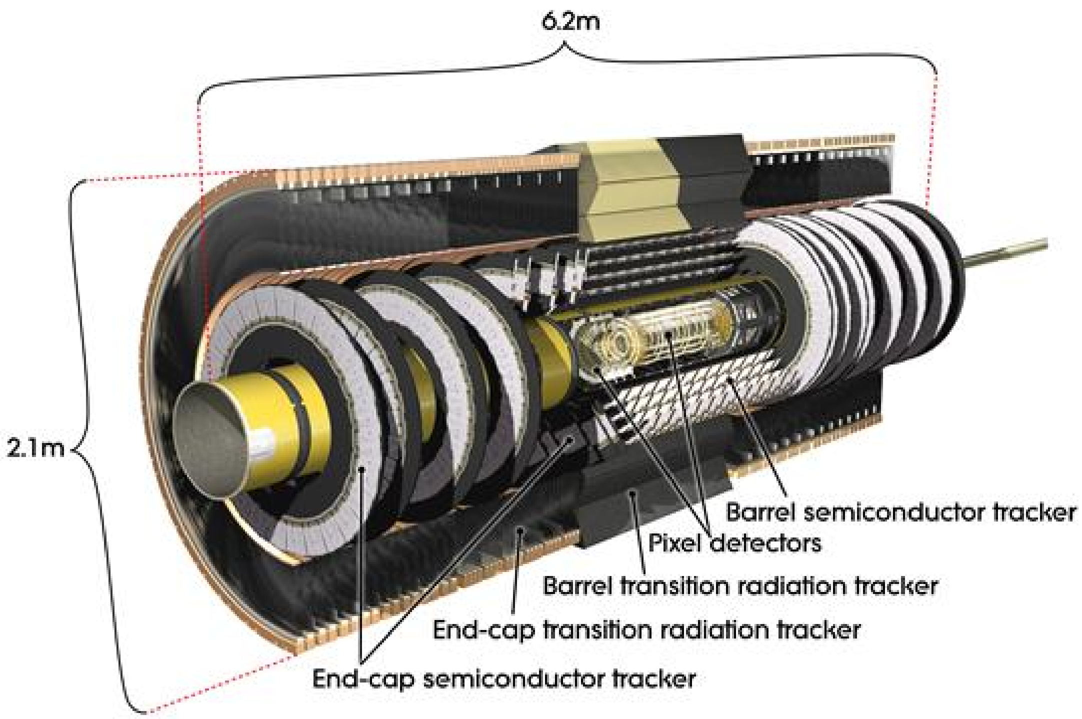

Figure 1.4: Cutaway view of the inner detector [13].

1.4.3 The calorimeter system

The calorimeter system is presented in Figure 1.5. Calorimeters enable to measure the energy of the particle passing through the detector. This measurement is associated with a production of an electromagnetic or hadronic particle shower. The ATLAS calorimeter system consist of an inner electromagnetic (EM) calorimeter and an external hadronic calorimeter. They both have alternately placed layers of passive (absorbing) and active materials. Electromagnetic calorimeters measure the energy of electrons and photos as they interact with matter. Hadronic calorimeter measure the energy of hadrons.

The electromagnetic barrel consist of lead as an absorbing material and copper electrodes. It uses liquid argon (LAr) as an active material. The hadronic barrel is build of alternately located plates of steel and scintillator. The end-cap region is divided into three components: lead-LAr electromagnetic end-cap (EMEC), copper-LAr hadronic end-cap (HEC) and forward calorimeter (FCal) composed of copper and tungsten layers working with LAr. The whole calorimeter system covers the pseudorapidity region $\eta \leq 4.9$.

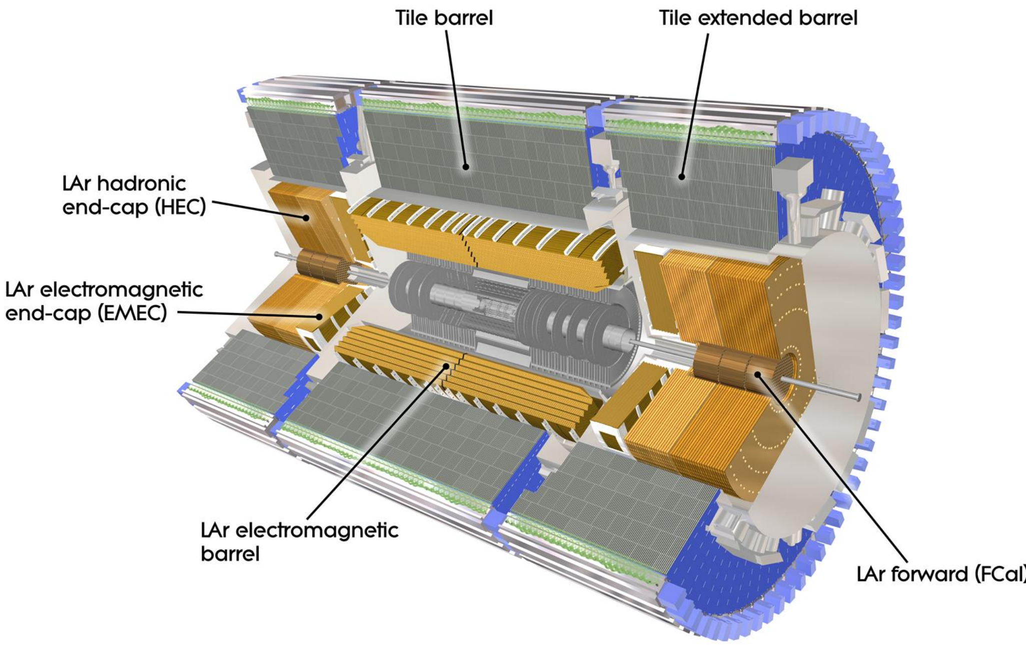

Figure 1.5: Cutaway view of the calorimeter system [13].

1.4.4 The muon spectrometer

Muons are able to penetrate all components of the detector described above. This group of particles requires a specific sub-detector surrounding the calorimeter system. The muon spectrometer (MS) consists of two types of triggering chambers and two types of precision tracking chambers as presented in Figure 1.6.

The triggering system includes the Resistive Plate Chambers (RPC) in the barrel region and the Thin Gap Chambers (TGC) in the end-caps. The RPCs are formed into three concentric layers. They are build of resistive bakelite plates spaced by insulating spacers. The volume between the plates is filled with gas mixture based on tetrafluoroethane (C2H2F4) and iso-butane (C4H10). The TGCs are build of anode wire plates and cathode plates covered with graphite. They are complemented with copper strips and pads providing readout channels. The chambers are filled with a gas mixture of CO_2 and n-pentane.

The tracking system consist of monitored drift tubes (MDT) and cathode strip chambers (CSC). The MDTs provide precise momentum measurement. They are arranged in three layers both in the barrel region and the end-caps. They consist of over 300 thousand drift tubes with a diameter of 3 cm filled with a mixture of Ar and CO_2 and the gold-plated tungsten wires in their centre. The CSCs are multiwire proportional chambers used for tracking in the endcaps. Their performance is also based on the gas mixture of Ar and CO_2 with tungsten-rhenium wires.

The integral part of the detector is a system of torodial superconducting magnets. The magnetic field enables measurement of muons momentum from their tracks curvature.

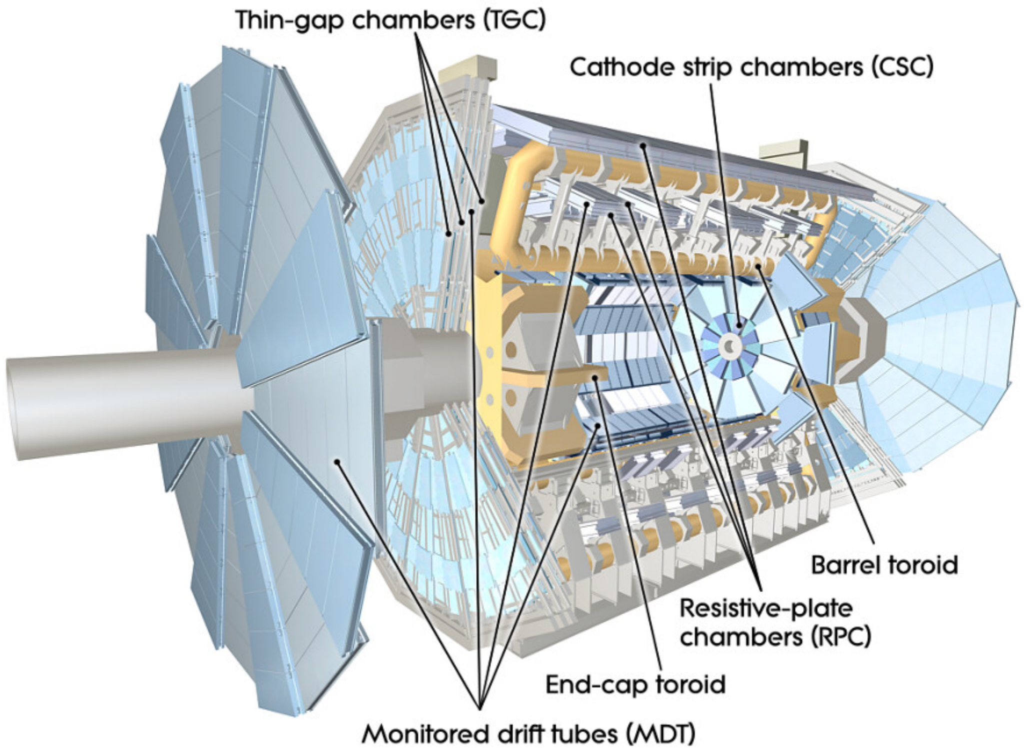

Figure 1.6: Cutaway view of the muon spectrometer [13].

1.4.5 The trigger system

The first step of the event selection is executed by the trigger system. It provides the basic data selection during the data collection - *online* and allows reducing the data-flow to manageable level. Trigger selection chooses events that are interesting for further *offline* analysis. The ATLAS trigger system consists of a hardware-based first-level trigger (L1) and a software-based high-level trigger (HLT). The L1 provides reduction of the data-taking rate to the maximum of approximately 100 kHz. It defines the regions of interest (ROIs) for further processing. Then, the HLT provides reduction of total data-taking rate to about 1 kHz. It uses offline reconstruction tools and fast algorithms to improve the L1 decisions.

2 | Background and signal Monte Carlo samples

2.1 Monte Carlo samples

Monte Carlo (MC) methods involve a wide range of computational algorithms based on random simulations for modelling complicated systems. High energy physics uses a variety of MC generators to simulate particle collisions and the detector response. Comparisons between the MC simulated events and the experimental data provide a deeper understanding of the real processes.

The MC samples production for the second LHC running period (Run II, years 2015 - 2018) has been divided into three sub-periods: *a, d* and *e*. This division is connected to the different pile-up conditions i.e. different number of proton-proton collisions during one bunch crossing at the LHC in different years of data taking. Signal and background samples used for the analysis were available only with two different pile-up settings which correspond to two data periods: 2015 - 2016 and 2017. During these data periods over 80 fb^{-1} events were collected in total.

2.1.1 Signal samples

The signal Monte Carlo samples were produced with the Herwig generator [14]. The cross-section of the di-Higgs production process for the final state considered in this thesis is $\sigma = 0.8643$ fb. The signal incorporates the possible decay modes containing WW, ZZ and $\tau\tau$ combinations. The signal simulation imposes a requirement on the existance of exactly two leptons in the final state (e, μ or τ decaying hadronically).

2.1.2 Background samples

The SM background processes faking the signal process are produced using different MC event generators. Each SM background process is normalised to the best available respective theoretical cross-section. For background modelling generators such as Pythia8 [15], Sherpa [16], Madgraph [17] and Powheg [18] were used. The event generation was then followed by a full simulation of the detector response for each event. The final state particles are processed through the Geant4 [19] simulation toolkit or the ATLAS fast simulation framework [20] - for the background MC samples Geant4 is used, and for signal MC samples it is replaced with the fast ATLAS calorimeter simulation. All the events from the simulation are then reconstructed using the same methods as for the data.

Background for di-Higgs production considered in presented studies includes production of gauge bosons pairs VV (WW, ZZ, WZ), three gauge bosons VVV (WWW, ZZZ, WWZ, WZZ), top quark pairs, top pair with gauge boson, W+jets, Z+jets, gauge boson with diphoton, as well as top quarks or gauge boson with single Higgs boson. The number of simulated background events is collected in Table 2.1.

Table 2.1: List of MC background processes and the number of simulated events used in the analysis.

Background process	Number of events
VV	44737600
VVV	132685
$t\bar{t}$	37397100
$t\bar{t}H$	7626470
$t\bar{t}V$	3183850
tV	449320
$V\gamma\gamma$	15657700
W+jets	76626300
Z+jets	27642900
VH	26397

3 | Object definitions and events preselection

Proton-proton collisions result in various processes. One of the aim of particle physics experiments is an event reconstruction. Each final state particle deposits its energy in a different part of the detector as shown in Figure 3.1. Reconstruction is a process of converting recorded electronic signals produced from the interactions of particles with detector material into information about the trajectory, momentum and charge of the particles. All this information is then combined to reconstruct objects such as photons, leptons or jets. The field of this analysis concentrates on the final state with one light lepton and one hadronically decaying τ. Therefore, the essential particles for the process described in this thesis are electrons, muons and taus. Some particular criteria were introduced to define these objects for further analysis.

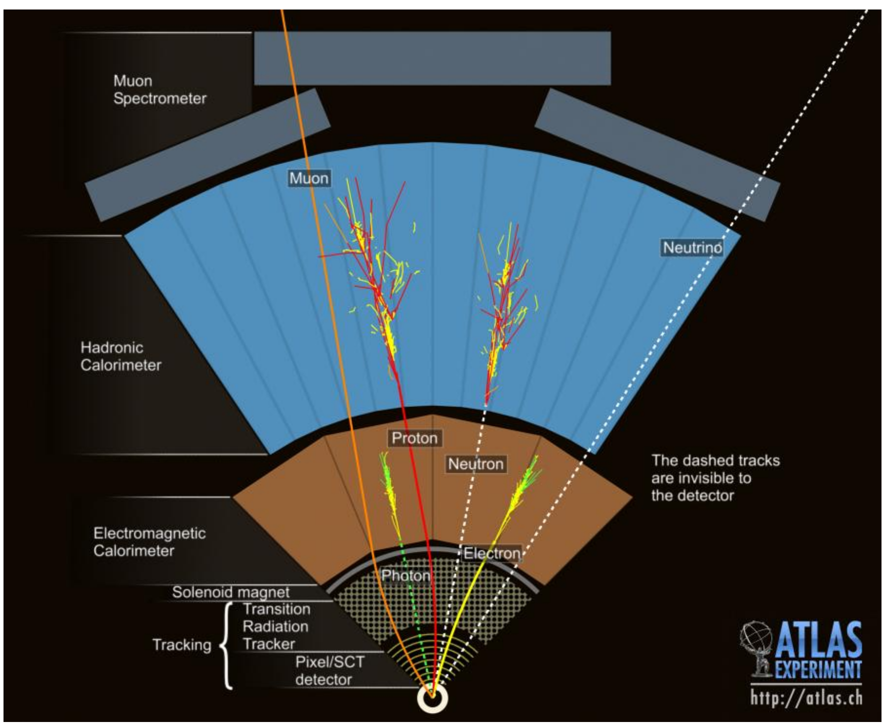

Figure 3.1: Cross-section of the ATLAS detector. Interactions of particles with different parts of the detector [21].

Three working points of identification are specified depending on the signal object identification efficiency and background rejection power: loose, medium and tight. Loose level provides the least restrictive criteria for fakes rejection but the highest efficiency for signal objects. Medium are more rigorous than loose, and tight selection applies the strictest conditions against background rejection.

3.1 Electrons

Electrons leave tracks in the inner detector and then initiate an electromagnetic showers travelling through the electromagnetic calorimeter. Thus they are reconstructed from energy clusters in the electromagnetic calorimeter associated with tracks reconstructed in the inner detector.

Applied selection for object definition of the electron is as follows:

(a) **ID = ± 1**
Reconstructed charge of an electron candidate. The charge determination is based on the analysis of the track's curvature reconstructed in the inner detector.

(b) $\boldsymbol{p_T \geq 10}$ **GeV** - transverse momentum of an electron candidate.

(c) $\boldsymbol{|\eta| < 2.5}$ and $\boldsymbol{1.37 < |\eta| < 1.57}$
The pseudorapidity region $1.37 < |\eta| < 1.57$ is called the *crack-region* and it corresponds to the region between the barrel and endcaps of the electromagnetic calorimeter. This range of η is characterized by a poor energy resolution and it needs to be excluded.

(d) $\boldsymbol{|z_0 sin\theta| < 0.5}$ and $\boldsymbol{d_0/\sigma(d_0) < 5}$
The z_0 and d_0 parameters are respectively the longitudinal and transverse impact parameters. The longitudinal impact parameter z_0 is defined as a difference between the z coordinate of the primary vertex and the point of the closest approach of the track in the z direction. The transverse impact parameter d_0 is defined as a distance of closest approach of the primary vertex point and the track in the transverse plane. Signal electrons need to satisfy the relation $d_0/\sigma(d_0) < 5$, where the transverse impact parameter d_0 is divided by its uncertainty $\sigma(d_0)$. Another requirement is $|z_0 sin\theta| < 0.5$, where the longitudinal impact parameter of the track is multiplied by the sine of the polar angle θ.

(e) **isolationFixedCutLoose requirement**
Prompt electron in signal process are isolated, contrary to non-prompt electrons in some backgrounds. There are two classes of isolation variables based on calorimeter and tracking measurements. The efficiency of loose fixed isolation criteria is about 98% [22].

(f) **isTrigMatch requirement**
An electron candidate should be matched with the one activating electron trigger.

The electron trigger used is unprescaled single lepton trigger with 26 GeV lowest p_T threshold.

(g) **chargeIDBDTMedium > 0.3**
To reduce charge misidentification, boosted decision trees (BDT) methods are used. It is possible to obtain the highest rejection of electrons with the wrong charge when the chargeIDBDTMedium parameter is greater than 0.3 [22].

Further, two different identification selections could be applied on electron candidates:

(a) **Medium selection**

- **MediumLH requirement**
  Identification of prompt electrons is based on likelihood (LH) method. Here the medium identification described in Ref. [23] is used.

(b) **Tight selection**

- **TightLH requirement**
  More restrictive requirement for electron identification than MediumLH requirement. Here the tight identification criterion described in Ref. [23] is used.
- $\boldsymbol{\frac{E_T^{cone20}}{p_T} < 0.06}$ and $\boldsymbol{\frac{p_T^{cone20}}{p_T} < 0.06}$
  In order to enhance the isolation criterion, two additional tight isolation cuts have been applied both on calorimeter isolation $\frac{p_T^{cone20}}{p_T}$ and track isolation $\frac{E_T^{cone20}}{p_T}$. The calorimeter isolation requires that the sum of transverse energies in a cone of ΔR = 0.2 around the lepton candidate divided by its transverse momentum p_T is less than 6%. The track isolation variable requires that the scalar sum of transverse momenta of all tracks in a cone of ΔR = 0.2 around the lepton candidate divided by its transverse momentum p_T is also less than 6%.

3.2 Muons

Muons travel through all the ATLAS detector components. They leave tracks in the inner detector, then run through calorimeters with little energy loss and finally reach the muon spectrometer. Therefore, the reconstruction of these particles use the information from the tracking system and the muon spectrometer.

Similarly to electrons, muons need to fulfil some particular criteria:

(a) **ID $= \pm$ 1** - reconstructed charge of a muon candidate.

(b) $\boldsymbol{p_T \geq}$ **10 Gev** - transverse momentum of a muon candidate.

(c) $\boldsymbol{|\eta| < 2.5}$ - pseudorapidity of a muon candidate.

(d) $\boldsymbol{|z_0 sin\theta| < 0.5}$ and $\boldsymbol{d_0/\sigma(d_0) < 5}$

(e) **isTrigMatch requirement**
A muon candidate should be matched with the one activating muon trigger. The muon trigger used is unprescaled single lepton trigger with 26 GeV lowest p_T threshold.

(f) **isolationFixedCutLoose requirement**
In order to extract isolated muons from the muons which are embedded in jets, a certain activity needs to be executed. Just as in case of electrons, the isolationFixedCutLoose requirement has been defined. The efficiency of this selection is greater than 96% [24].

Further, two different identification selections could be applied on muon candidates:

(a) **Medium selection**

- **Medium** requirement on muon identification as defined in Ref. [24].

(b) **Tight selection**

- **Tight** requirement on muon identification as defined in Ref. [24].
- $\boldsymbol{\frac{p_T^{cone20}}{p_T} < 0.06}$ - tighter selection on isolation, as for electron candidates.

3.3 Taus

Although τ particle is a lepton, it meaningfully differs from electrons and muons in that it can decay into hadrons. It has a lifetime of 2.9 $\cdot 10^{-13}$ s [6]. Therefore, it decays just before reaching the first part of the detector. As a result it is not possible to detect it directly - it is not marked in Figure 3.1. Only τ decay products enable its identification. It decays leptonically approximately 35% of the time and hadronically approximately 65% of the time. Table 3.1 shows leptonic and hadronic tau decays and their branching ratios. In hadronic case, the decay contains one or three charged pions. Experimentally distinguishing between electrons and muons originating from τ decays and prompt electrons and muons is very difficult. Only hadronically decaying τ is considered in presented analysis. Such decays are seen in the detector as narrow jets in both electromagnetic and hadronic calorimeters. Thus their reconstruction is seeded by jets in the calorimeters. The charge of a τ candidate is calculated from sum of charges of the attached tracks.

Table 3.1: Branching ratios of leptonic and dominant hadronic τ decays [6].

leptonic decays	BR [%]	hadronic decays	BR [%]
$\mu^-\overline{\nu}_\mu\nu_\tau$	17.39	$\pi^-\pi^0\overline{\nu}_\tau$	25.49
$e^-\overline{\nu}_e\nu_\tau$	17.89	$\pi^-\nu_\tau$	10.81
		$\pi^-\pi^0\pi^0\nu_\tau$	9.26
		$\pi^-\pi^-\pi^+\nu_\tau$	8.99
		$\pi^-\pi^-\pi^+\pi^0\nu_\tau$	2.74
		$\pi^-\pi^0\pi^0\pi^0\nu_\tau$	1.04

The tau objects are defined by the following selection:

(a) **passEleBDT** and **passMuonOLR** requirements
Tau candidate is possible to be misidentified with a light lepton. These two parameters referring to electrons and muons respectively, enables to discard tau candidates if they overlap with a light lepton.

(b) **numTrack= 1 or numTrack = 3**
The number of tracks associated with a tau candidate is required to be one or three.

(c) $|\boldsymbol{\eta}| < \mathbf{2.5}$ **and** $\mathbf{1.37} < |\boldsymbol{\eta}| < \mathbf{1.57}$ - pseudorapidity of a tau candidate.

(d) Two different identification criteria can be applied on selected tau candidate:

- **JetBDTSigMedium** with medium identification criterion as defined in Ref [25].
- **JetBDTSigTight** with tight identification criterion as defined in Ref [25].

3.4 Event preselection

This analysis describes a search for Higgs boson pair production in multi-lepton final state. The following event selection criteria are applied.

(a) Exactly one electron or muon candicate after selection described in Sec. 3.1 and 3.2.

(b) Exactly one tau candicate after selection described in Sec. 3.3

(c) **b-jets veto**
One of the background is $t\bar{t}$ production. Top quarks decay into Wb final state. B-tagging techniques identify jets originating from b quark. Vetoing events with b-tagged jets rejects background coming from top quarks.

(d) **nJets** $\geq$ **2**
The number of jets in the final state is required to be at least 2.

Three combinations of medium and tight operating points for light leptons and taus were considered to choose the most efficient one. Following combinations were tested: medium light lepton and medium tau, tight light lepton and medium tau, tight light lepton and tight tau.

Table 3.2 shows the number of events passing the object selection and the event preselection cuts (for different working points) with the values of efficiencies of each cut. The overall number of background events including each background processed is 213 480 322 and the overall number of signal events processed is 288 882. The dominant background processes are productions of gauge boson pairs, top pairs and W bosons with jets.

Table 3.2: The number of total background and signal events passing the object selection with the corresponding efficiencies.

	Background		Signal	
	number of events	efficiency [%]	number of events	efficiency [%]
b-jets veto	160123603	75.01	255272	88.37
nJets ≥ 2	77978800	36.53	233445	80.81
medium light lepton and medium tau	1996732	0.94	33510	11.60
tight light lepton and medium tau	1425255	0.67	23222	8.04
tight light lepton and tight tau	964353	0.45	18522	6.41

4 | Analysis

4.1 Signal to background ratio

For different cuts on transverse momentum p_T signal to square–root background ratio $\frac{S}{\sqrt{B}}$ has been calculated. The main aim is to maximize this ratio. All $\frac{S}{\sqrt{B}}$ plots, as well as subsequent plots have been normalised to the number of expected events based on the cross section and luminosity. Cuts of $p_T \geq 20$, 25, 30, 35, 40, 45, 50, 55 GeV has been applied for either light leptons or taus.

The final states of any process involving a combination of charged particles implicate taking their charges under consideration. Thus analysed events were splitted into two categories: events containing particles with the same - $l^{\pm}\tau^{\pm}$, or the opposite sign - $l^{\pm}\tau^{\mp}$, where $l = e/\mu$.

The result of $\frac{S}{\sqrt{B}}$ calculations with different combinations of p_T cuts is presented in Figures 4.1 - 4.3. Red-marked areas relate to the highest scores of $\frac{S}{\sqrt{B}}$ calculations. Both opposite-sign and same-sign categories were investigated as well as a merged category.

As shown in Figures 4.1 - 4.3 the highest $\frac{S}{\sqrt{B}}$ value is achieved for both light lepton and τ satisfying medium working point. Applying tight selection criteria reduces the number of signal events. For this reason it is sufficient to choose the medium selection working point. The SS events have a small contribution to the overall number of events without sign specification. The optimal cuts were found to be the 25 GeV cut on light lepton transverse momentum and the 45 GeV cut on tau transverse momentum. For higher cuts on tau transverse momentum the number of signal events is significantly reduced.

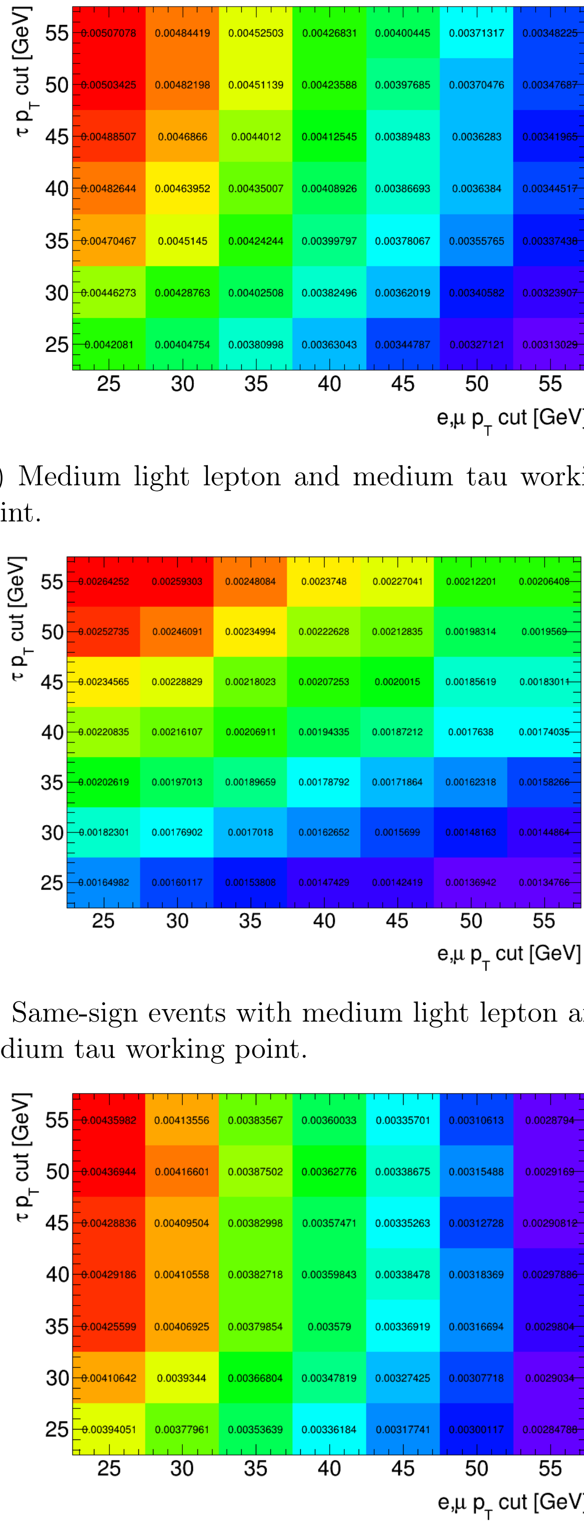

(a) Medium light lepton and medium tau working point.

(b) Same-sign events with medium light lepton and medium tau working point.

(c) Opposite-sign events with medium light lepton and medium tau working point.

Figure 4.1: Distributions of $\frac{S}{\sqrt{B}}$ values for different p_T cut combinations.

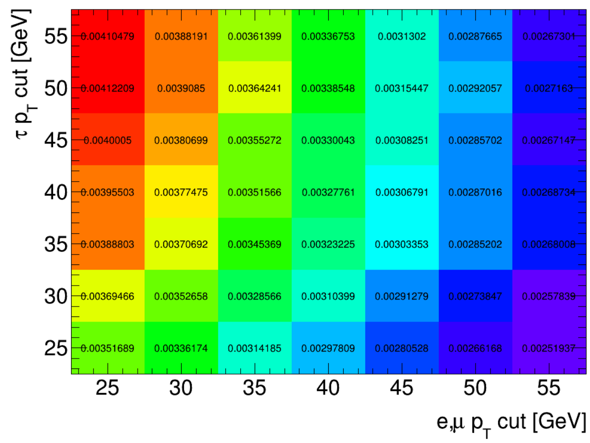

(a) Tight light lepton and medium tau working point.

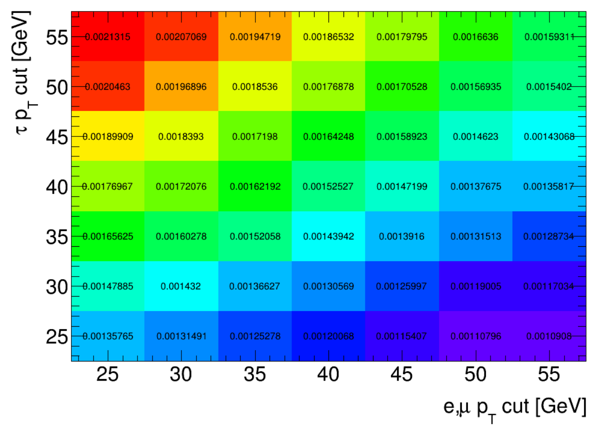

(b) Same-sign events with tight light lepton and medium tau working point.

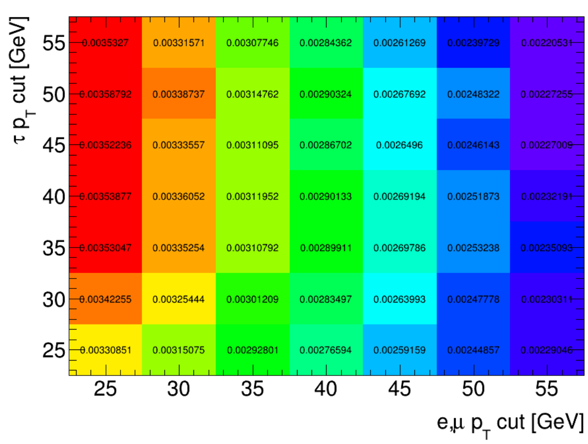

(c) Opposite-sign events with tight light lepton and medium tau working point.

Figure 4.2: Distributions of $\frac{S}{\sqrt{B}}$ values for different p_T cut combinations.

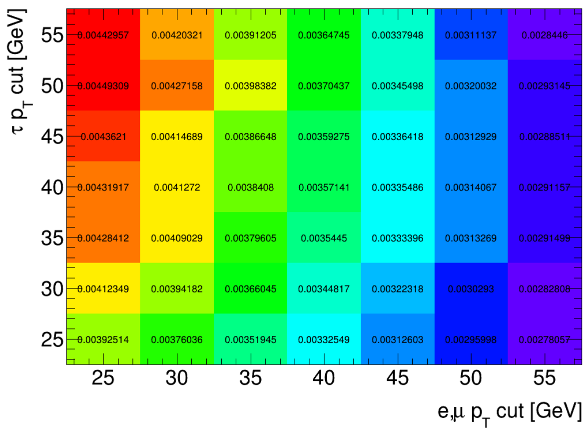

(a) Tight light lepton and tight tau working point applied.

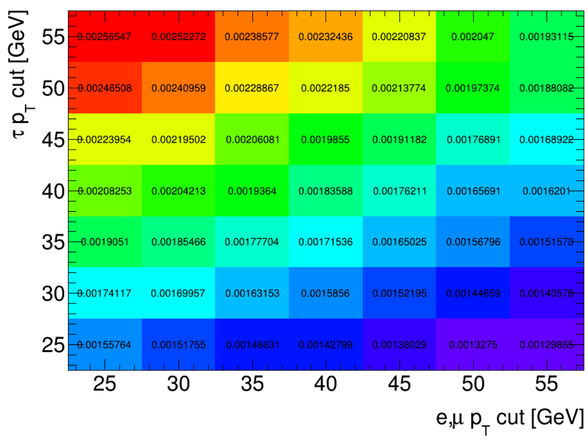

(b) Same-sign events with tight light lepton and tight tau working point applied.

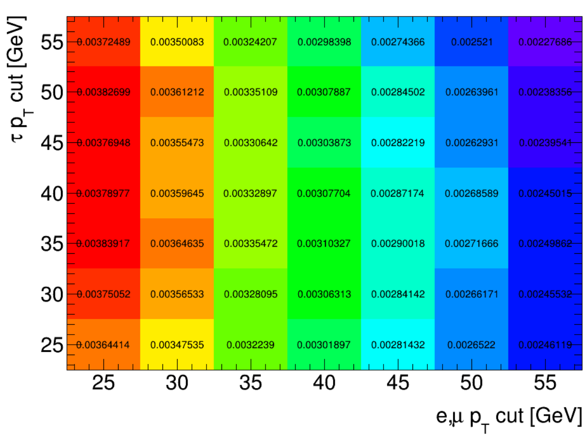

(c) Opposite-sign events with tight light lepton and tight tau working point applied.

Figure 4.3: Distributions of $\frac{S}{\sqrt{B}}$ values for different p_T cut combinations.

4.2 Results

Plots in Figures 4.4 and 4.5 are obtained as a result of applying the event selection criteria described in Section 3. Figures 4.4a and 4.4b depict the distribution of the transverse momentum of light leptons and taus respectively. Figures 4.4c and 4.4d present the distributions of light leptons η and ϕ.

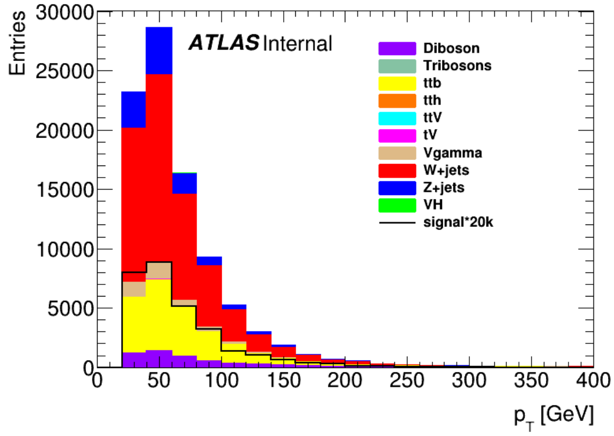

(a) Light leptons transverse momentum.

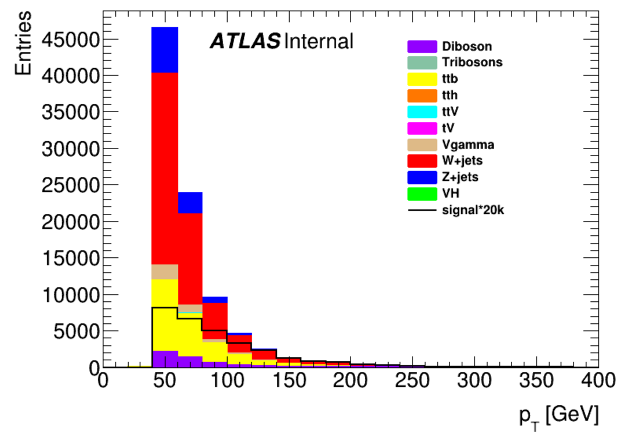

(b) Taus transverse momentum.

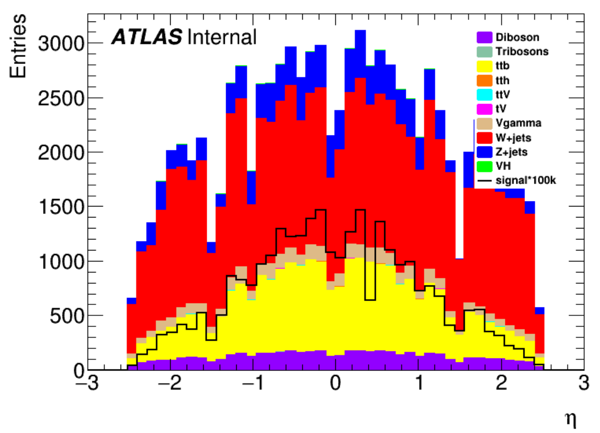

(c) Light leptons η.

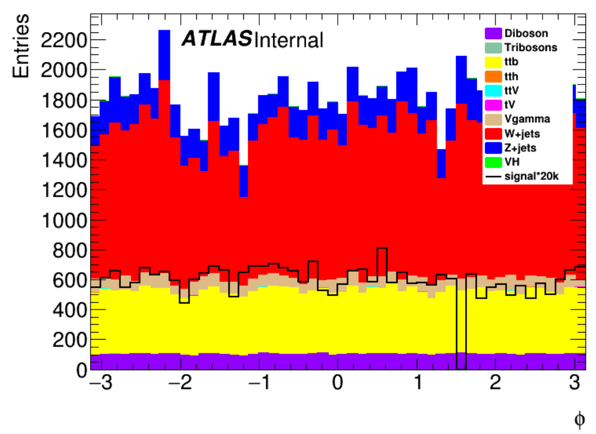

(d) Light leptons ϕ.

Figure 4.4: Distributions of the selected objects transverse momenta and η and ϕ of light leptons for the predicted backgrounds and signal. All signal distributions were scaled by factor 20 000.

Figure 4.5a presents the distribution of the visible mass of the system consisting of one light lepton and one tau. It does not include the mass of escaping neutrinos.

Figures 4.5b and 4.5c show the distributions of difference between light lepton and tau in η, $\Delta\eta_{l,\tau} = \eta_l - \eta_\tau$, and in ϕ, $\Delta\phi_{l,\tau} = \phi_l - \phi_\tau$. These variables were used to determine the distance between the light lepton and the tau, $\Delta R_{l,\tau} = \sqrt{\Delta\eta_{l,\tau}^2 + \Delta\phi_{l,\tau}^2}$, presented in Figure 4.5d. In Figure 4.5e the distribution of the number of jets in the final state is presented.

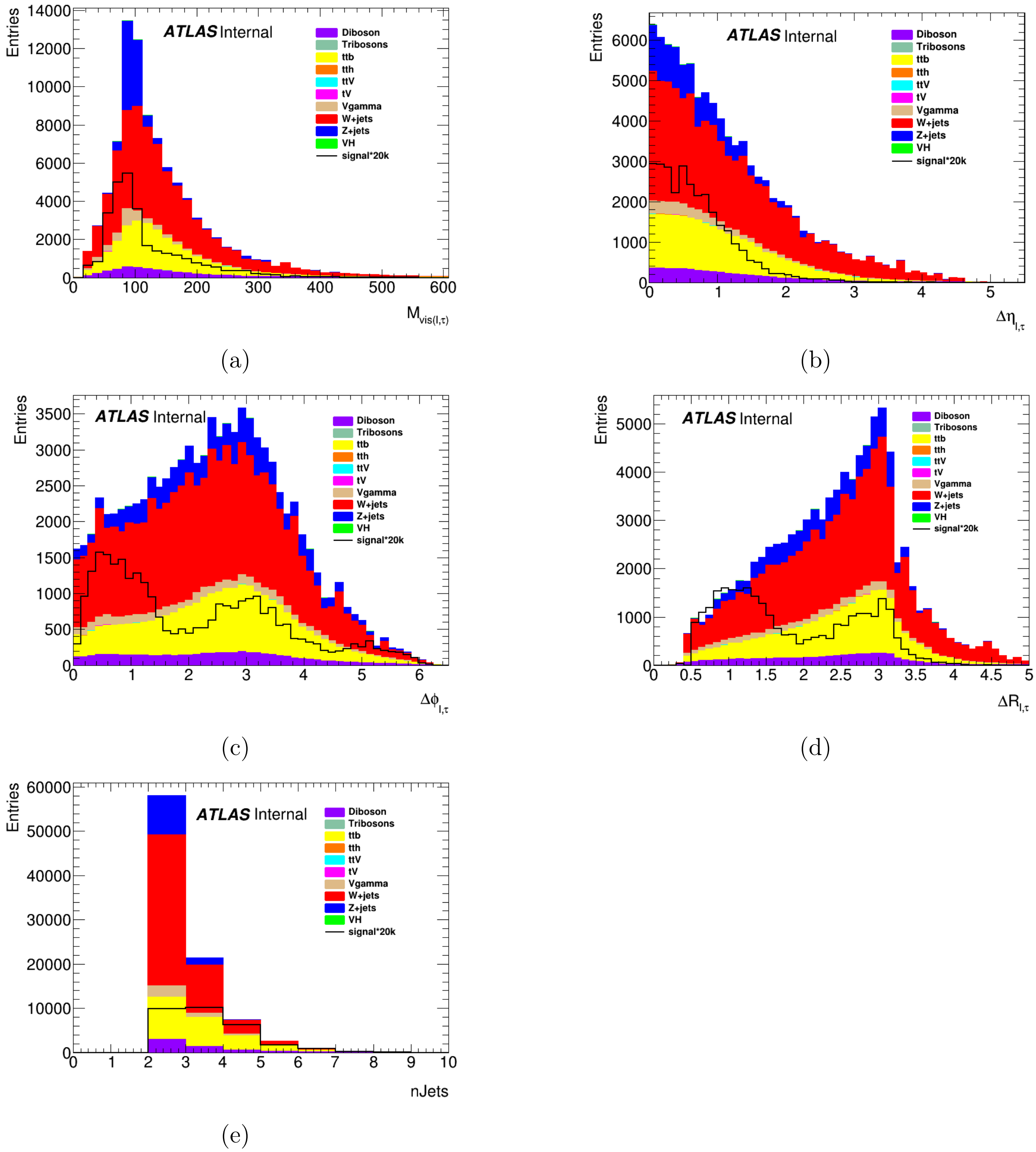

Figure 4.5: Distributions of the selected light lepton and tau visible mass (a), difference between light lepton and tau in η (b), in ϕ (c), their cone distance $\Delta R_{l,\tau}$ (d) and distribution of the number of jets (e) for the predicted backgrounds and signal. All signal distributions were scaled by a factor of 20 000.

Distributions presented in Figures 4.5 show possibility for applying additional cuts towards better background rejection. Looking at the distribution of the number of jets one can notice that the number of jets in background is lower than in signal events. This fact motivates to apply the cut on the number of jets: nJets > 2. The efficiency of this cut is 52% for signal and 21% for background. The $\frac{S}{\sqrt{B}}$ ratio after that cut increases from 0.00489 $\pm$ 0.00003 to 0.00540 $\pm$ 0.00004.

In Figure 4.6 the distribution of $\Delta R_{l,\tau}$ after applying nJets>2 cut is presented.

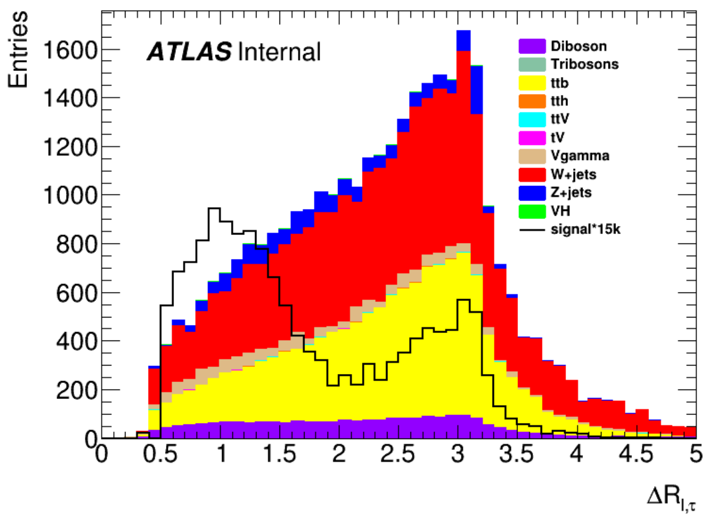

Figure 4.6: Distribution of $\Delta R_{l,\tau}$ after application of the nJets>2 cut for predicted background and signal. The signal distribution is scaled by a factor of 15 000.

The further selection is performed with the $\Delta R_{l,\tau} < 2$ requirement. This arbitrary chosen cut gives a good separation between the background and the signal events. The efficiency of this cut is 38% for signal and only 9% for background. Figure 4.7 shows the distributions of $\Delta R_{l,\tau}$ and the invariant mass of one light lepton and one τ after the two above selections. The final $\frac{S}{\sqrt{B}}$ ratio is 0.00587 $\pm$ 0.00004. The $\frac{S}{\sqrt{B}}$ is small as the SM cross section for di-Higgs production is assumed. It has to be stressed that obtained optimisation results are independent from assumed di-Higgs production cross-section. However, in BSM searches the cross section for di-Higgs production is enhanced and the $\frac{S}{\sqrt{B}}$ will be much more higher.

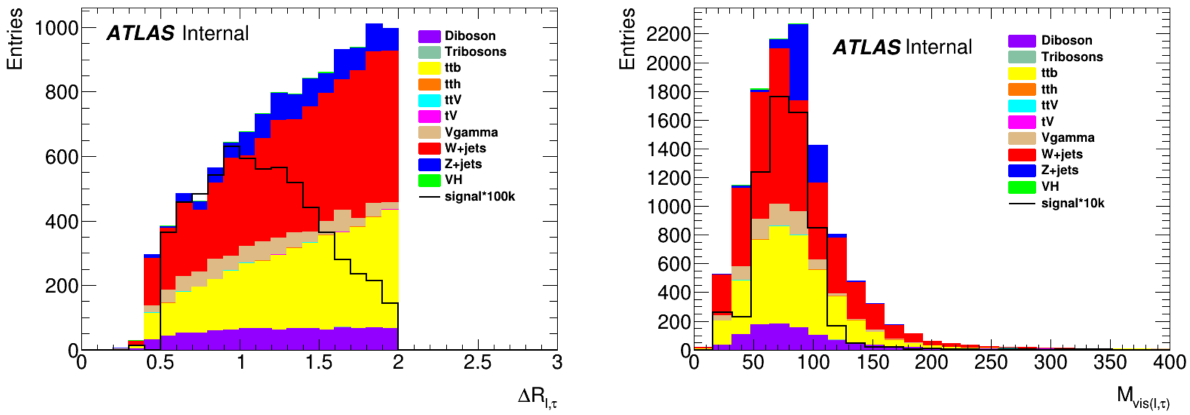

(a) (b)

Figure 4.7: The distributions of $\Delta R_{l,\tau}$ (a) and visible mass of light lepton and tau (b) after application of nJets>2 and $\Delta R_{l,\tau} < 2$ cuts for predicted background and signal. The signal distributions are scaled by a factor of 10 000.

The number of signal and background events passing all final requirements are summarized in Table 4.1.

Table 4.1: The number of signal and background events passing all event selection criteria.

	object definition	$p_T^{lep} > 25$ GeV $p_T^{tau} > 45$ GeV	nJets >2	ΔR<2
signal events	33510	23979	17318	12615
background events	1996732	859638	426524	182064

Efficiencies of all the final selection cuts are presented in Table 4.2.

Table 4.2: The efficiency of the final selection.

	$p_T^{lep} > 25$ GeV $p_T^{tau} > 45$ GeV	nJets >2	ΔR<2
signal events	71%	52%	38%
background events	43%	21%	9%

The distribution of $\Delta R_{l,\tau}$ (Figure 4.7a) achieved as a result of the chosen selection was used for the determination of the limit on the di-Higgs production cross section. The $\Delta R_{l,\tau}$ distribution shows larger difference between the shape of the signal and the shape of the background in comparison to the distribution of the visible mass of light lepton and tau. The limit arises from the profile likelihood ratio fit for the background-only and the background with signal hypothesis with the $\Delta R_{l,\tau}$ as the discriminating variable. There are no systematic uncertainties considered. The obtained upper limit is set to 0.688247 pb.

5 | Conclusions

Presented analysis concerns a search for production of di-Higgs in multileptonic final state including one light lepton and one tau lepton. This channel has never been investigated by the ATLAS collaboration. Thus, presented analysis is a pioneer work. The upper limit on the cross-section for the di-Higgs process in analysed channel is set to 0.688247 pb. The obtained $S/\sqrt{B}$ ratio after the full selection is 0.00587 ± 0.00004. However, background considered in the analysis contains only SM processes. The QCD background was not included as it can be estimated only by data-driven techniques and processed data was not available at the time of performing presented studies. The impact of the QCD background can be significant due to high probability if misidentification of QCD jets as tau candidates and additional cuts have to be developed for its rejection. Also in presented studies no systematic uncertainties were considered. For completeness, the upper observed limit on di-Higgs production cross-section in the $b\bar{b}b\bar{b}$ final state, the one with the highest BR, is 1.22 pb [26].

Despite of the outcome not featuring the full information, obtained results are promising. The analysed final state can improve the overall limits on di-Higgs production together with complementary multileptonic final states. Subsequent studies are planned to include the QCD background estimation and following cuts optimisation.

Bibliography

[1] D.J. Griffiths, *Introduction to Elementary Particles*, John Wiley & Sons, 1987.

[2] The ATLAS Collaboration, *Observation of a New Particle in the Search for the Standard Model Higgs Boson with the ATLAS Detector at the LHC*, Phys.Lett. B 716 (2012) 1-29.

[3] The CMS Collaboration, *Observation of a new boson at a mass of 125 GeV with the CMS experiment at the LHC*, Phys. Lett. B 716 (2012) 30.

[4] L. Evan, P. Bryant (editors), *LHC Machine*, an abridged version of the LHC Design Report (CERN-2004-003).

[5] T. Rothman, S. Boughn *Can Gravitons Be Detected?*, Found.Phys. 36 (2006) 1801-1825.

[6] Review of Particle Physics, M. Tanabashi et al. (Particle Data Group), Phys. Rev. D 98, 030001 (2018).

[7] The ATLAS and CMS Collaborations, *Combined Measurement of the Higgs Boson Mass in pp Collisions at $\sqrt{s} = 8$ TeV with ATLAS and CMS Experiments*, Phys. Rev. Lett. 114 (2015) 191803.

[8] F. Englert and R. Brout, Phys. Rev. Lett. 13, (1964) 321; P. W. Higgs, Phys. Lett. B12, (1964) 132; P. W. Higgs, Phys. Rev. Lett. 13, (1964) 508.

[9] S. Di Vita et al., *A global view on the Higgs self-coupling*, JHEP 1709 (2017) 069.

[10] The ATLAS Collaboration, *Search for non-resonant Higgs boson pair production in the $bb'\nu'\nu$ final state with the ATLAS detector in pp collisions at $\sqrt{s} = 13$ TeV*, Phys. Lett. B 801 (2020) 135145.

[11] The ATLAS Collaboration, *Measurements of the Higgs boson production and decay rates and coupling strengths using pp collision data at $\sqrt{s} = 7$ and 8 TeV in the ATLAS experiment*, Eur. Phys. J. C76 (2016) 6.

[12] The ATLAS Collaboration, *Combination of searches for Higgs boson pairs in pp collisions at $\sqrt{s} = 13$ TeV with the ATLAS detector*, Phys. Lett. B 800 (2020) 135103.

[13] The ATLAS Collaboration, *The ATLAS Experiment at the CERN Large Hadron Collider*, Eur. Phys. J. C76 (2016) 6.

[14] M. Bahr et al., *Herwig++ Physics and Manual*, Eur.Phys.J.C58:639-707, 2008.

[15] T. Sjöstrand, S. Mrenna, P. Skands, *A Brief Introduction to PYTHIA 8.1*, Comput. Phys. Commun. 178:852-867,2008.

[16] T. Gleisberg et al., *Event generation with SHERPA 1.1*, JHEP 02 (2009) 007.

[17] J. Alwall et al., *The automated computation of tree-level and next-to-leading order differential cross sections, and their matching to parton shower simulations*, JHEP07(2014)079.

[18] S. Alioli et al., *A general framework for implementing NLO calculations in shower Monte Carlo programs: the POWHEG BOX*, JHEP 06 (2010) 043.

[19] GEANT4 collaboration, *GEANT4 – a simulation toolkit*, Nucl. Instrum. Meth. A 506 (2003) 250.

[20] The ATLAS Collaboration, *The ATLAS simulation infrastructure*, Eur. Phys. J. C70 (2010) 823.

[21] CERN Document Server, CERN-GE-0803022,
URL: https://cds.cern.ch/record/1096081, [access: 20.12.2019].

[22] The ATLAS Collaboration, *Electron reconstruction and identification in the ATLAS experiment using the 2015 and 2016 LHC proton–proton collision data at* $\sqrt{s} = 13$ *TeV*, Eur. Phys. J. C 79 (2019) 639.

[23] The ATLAS Collaboration, *Electron and photon performacance measurements with the ATLAS detector using the 2015-2017 LHC proton-proton collision data*, JINST 14 (2019) P12006.

[24] The ATLAS Collaboration, *Muon reconstruction performance of the ATLAS detector in proton–proton collision data at* $\sqrt{s} = 13$ *TeV*, Eur. Phys. J. C 76 (2016) 292.

[25] The ATLAS Collaboration, *Measurement of the tau lepton reconstruction and identification performance in the ATLAS experiment using pp collisions at* $\sqrt{s} = 13$ *TeV*, ATLAS-CONF-2017-029.

[26] The ATLAS Collaboration, *Search for pair production of Higgs bosons in the* $b\bar{b}b\bar{b}$ *final state using proton–proton collisions at* $\sqrt{s} = 13$ *TeV with the ATLAS detector*, JHEP 01 (2019) 030.